Supporting Information

Size-controlled, hollow and hierarchically porous Co_2Ni_2 alloy nanocubes for efficient oxygen reduction in microbial fuel cells

Wenyi Wang[a],Xueqin Wang[a], Yuanyuan Wang[a], Bolong Jiang[b], Hua Song[a,*]

a. Provincial Key Laboratory of Oil & Gas Chemical Technology, College of Chemistry & Chemical Engineering, Northeast Petroleum University, Daqing 163318, Heilongjing, China.

b. Innovation Institute for Sustainable Maritime Architecture Research and Technology, Qingdao University of Technology, Qingdao 266000, Shandong, China.

* Corresponding author. Tel/Fax: +86 0459 6503167

E-mail: songhua2004@sina.com (Hua Song).

Structure and Composition

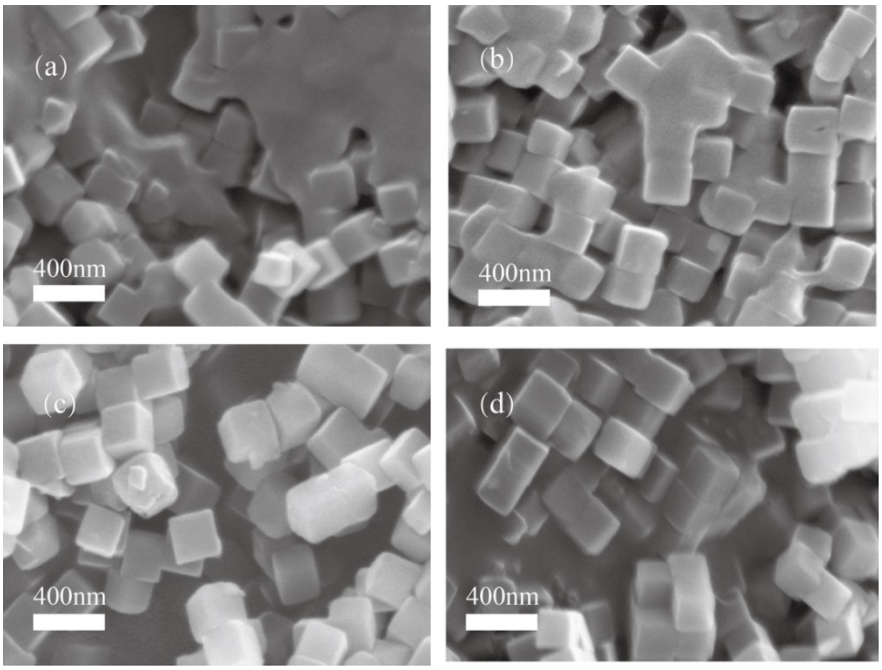

Figure S1 Representative SEM images of the products collected from the reaction in the synthesis of porous Co_2Ni_2 ANCs obtained at 90 °C (a), 100 °C (b), 110 °C (c) and 120 °C(d), respectively.

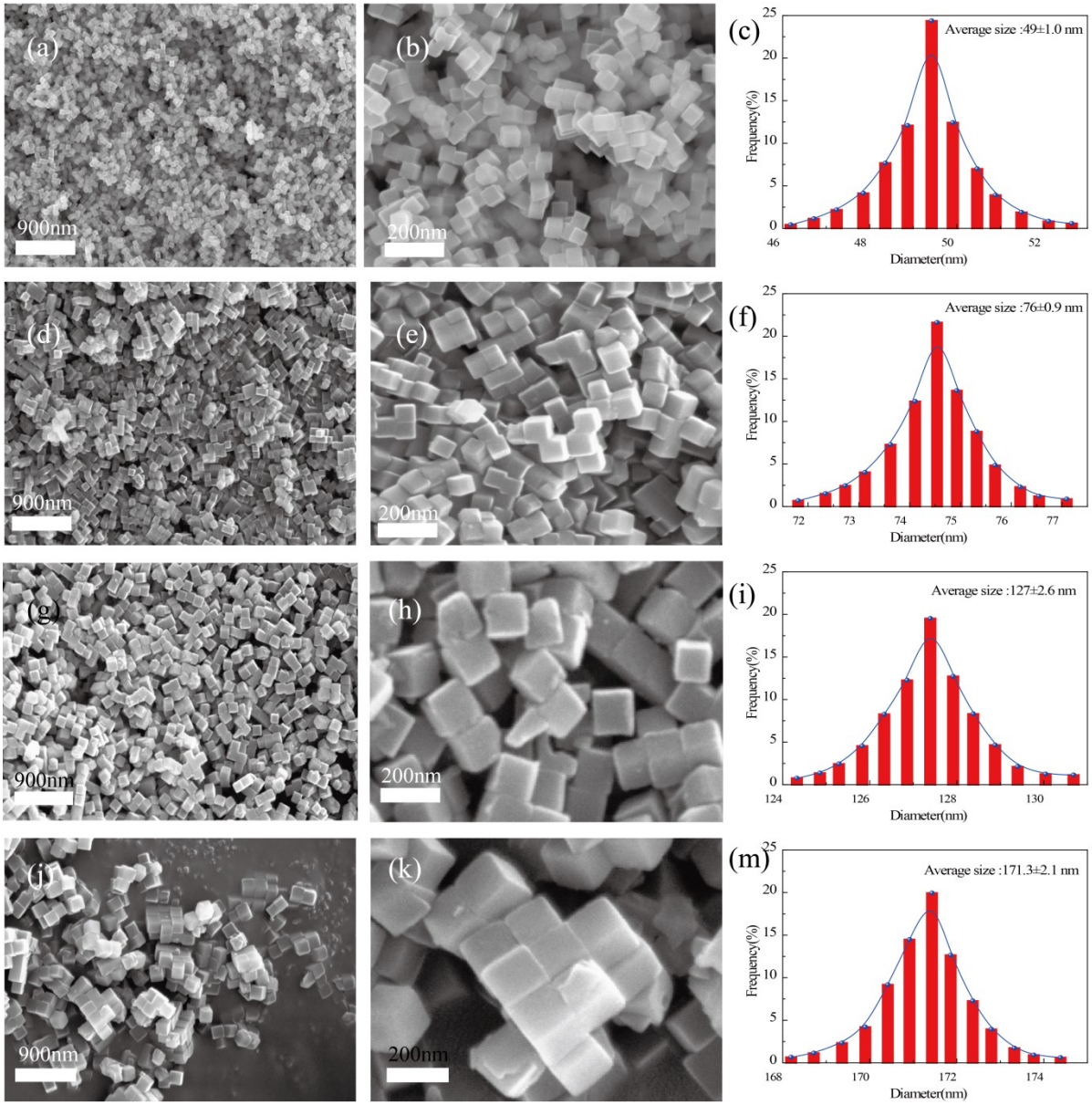

Figure S2 Representative SEM images and diameter distributions of the products collected from the reaction in the synthesis of porous Co_2Ni_2 ANCsprepared at 110°C for 1h(a-c), 2h(d-f), 3h(g-i) and 4h(j-m), respectively.

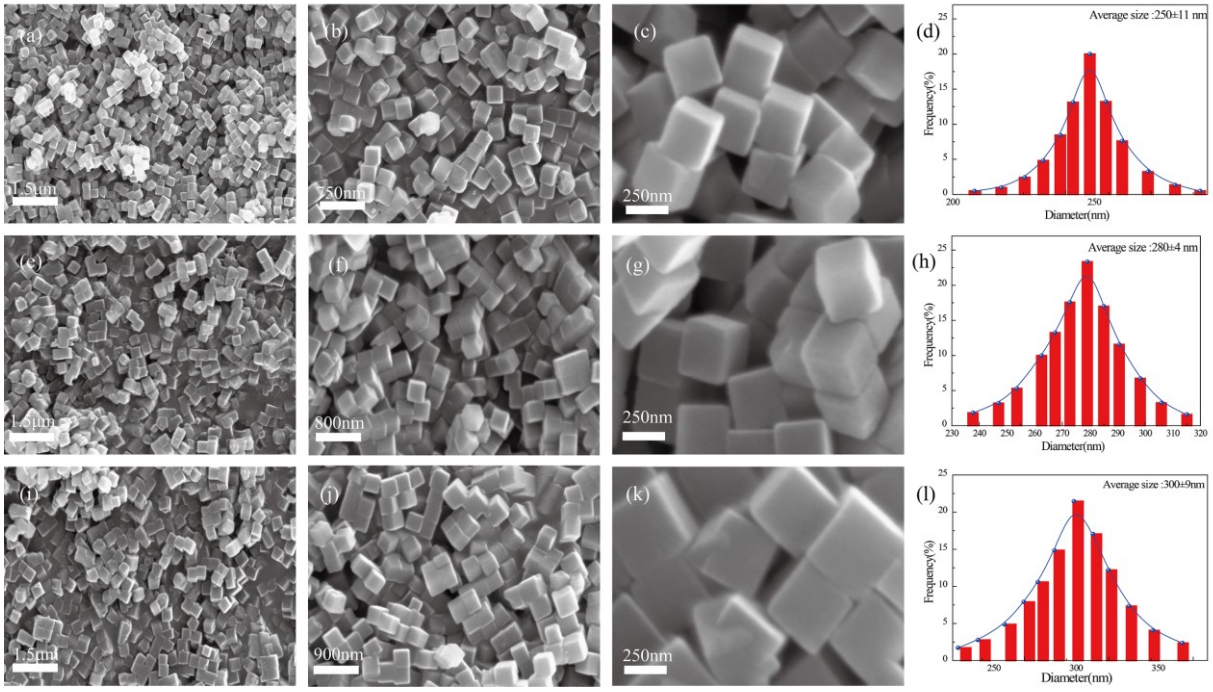

Figure S3 Representational SEM pictures and the distributions of diameter of size-controlled of hierarchically porous binary Co_2Ni_2 ANCs by the addition content of DMF solution of urea ((a-c, d): 10 mL; (e-g, h):15 mL; (i-k, l):20 mL).

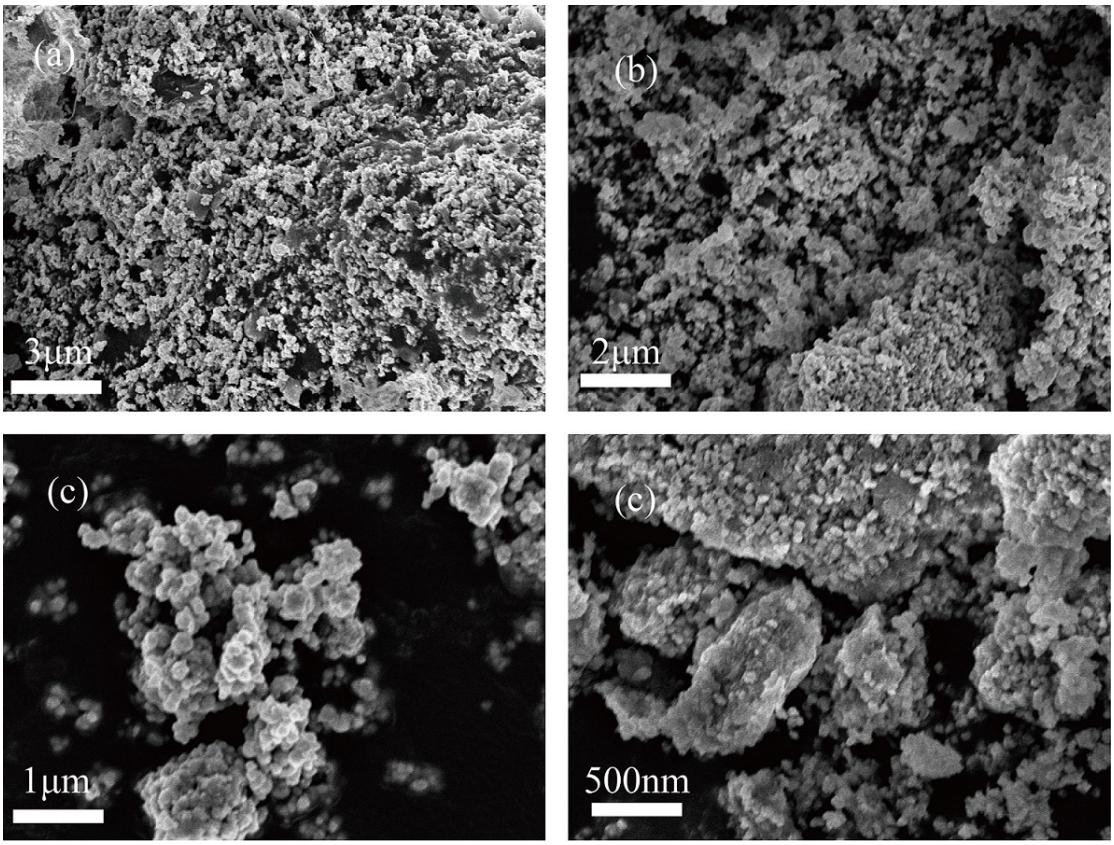

Figure S4 Representational SEM pictures and the distributions of diameter of Co_2Ni_2 particles prepared by the same condition used in the synthesis of porous Co_2Ni_2 ANCs without DMF solution of urea. It is proved that in the absence of the addition of structural guiding agent, the alloy material can not be self-assembled into a regular, but only by co-reduction to become chaotic nanoparticles, and agglomeration occurs in a large area.

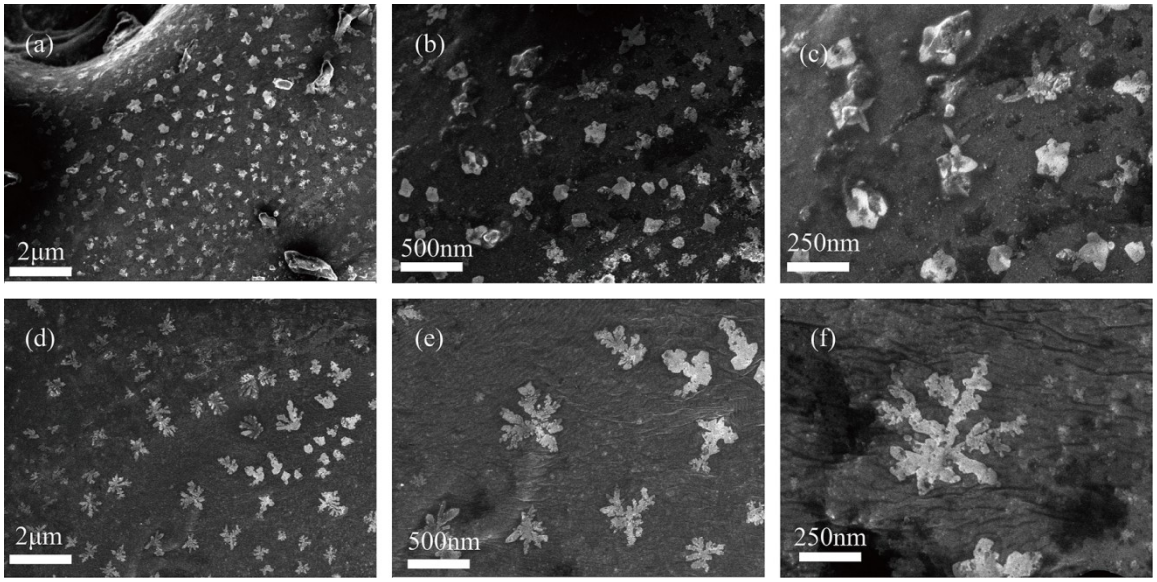

Figure S5 Representative SEM images of the products collected from the reaction with the same condition used in the synthesis of porous Co_2Ni_2ANCs with changing urea into, CTAB (a-c) and PVP (d-f). It was found that the morphological structure of the Co_2Ni_2 ANCs presented a completely different consequence with orderly arranged four-pointed stars with a 50nm average diameter (a-c) and an intact branch with a 500nm average diameter (d-f). The reason why the nanocubes fail to assemble successfully and form other morphologies may be that they do not form a weakly alkaline system.

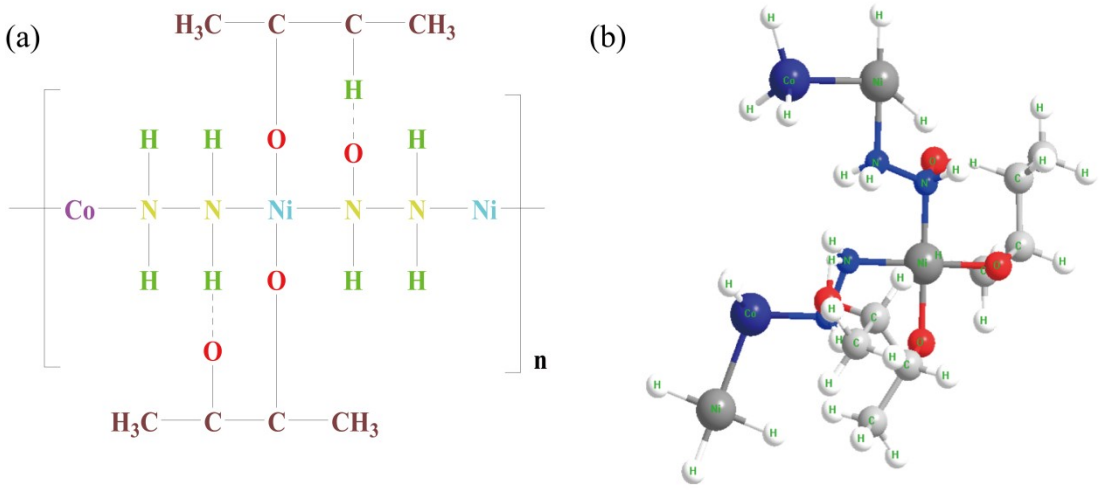

Figure S6 The connection type of $[CoNi(N_2H_4)_2(acac)_2]_n$ complexe.

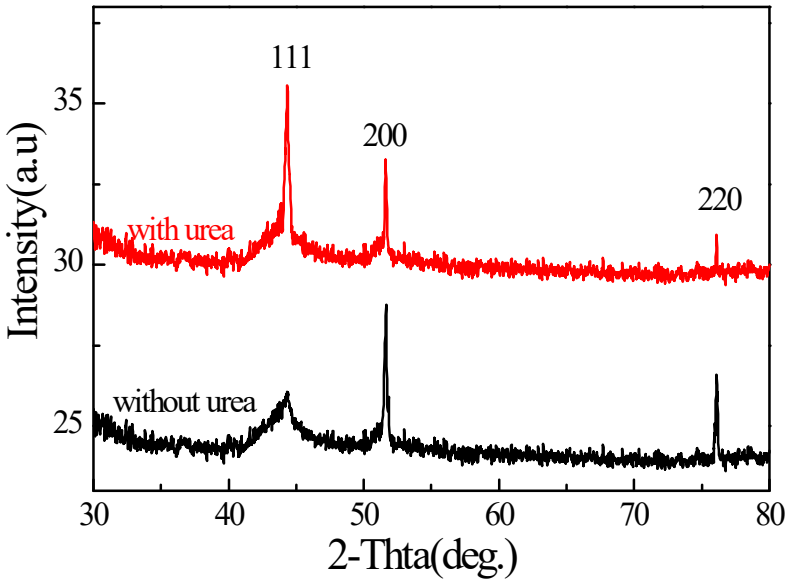

Figure S7 The XRD patterns of Co_2Ni_2 alloy prepared by the addition of urea and no urea.

To gain further details of synthesis process for Co_2Ni_2 ANCs, representative SEM images of the transformation process for different temperatures are shown in Fig. S1. The nanocube structure of the products already emerged with aggregation but weakly decentralized at lower synthesis temperatures. However, higher synthesis temperatures resulted in uneven dispersion. Besides, time-dependent experiments were conducted at 110°C for different synthesis time, and representative SEM images of the products obtained from various time are shown in Fig. S2. The cubic structure of Co_2Ni_2 alloy formed in the initial stage (1h) possesses 49±1.0nm inside length. With the prolongation of the synthesis time, the size of the Co_2Ni_2 nanocube gradually increased, indicating the Co_2Ni_2 crystals grew from the original small cubes along their edges. In addition, the effect of DMF solution amount was studied, unexpectedly, the average side length of the Co_2Ni_2 ANCs increased from ~200 to ~300 nm, with increasing DMF solution of urea from 5 to 20 mL, as shown in Fig. S3. This is possibly because the amount of DMF solution affects the urea content as well as the concentration of hydrazine hydrate in the system, which in turn affects the reduction reaction and crystal nucleate growth rate. Therefore, the average size of the Co_2Ni_2 ANCs could be precisely controlled by regulating the amount of DMF solution with positive correlation.

The urea was considered to play a role of structure-directing modulator, since without the use of urea, the nanocubes could not be obtained but only the irregular and randomly sized Co_2Ni_2 particles were formed (Fig. S4). To replace the urea with other structure-directing modulators of such as hexadecyltrimethylammonium bromide (CTAB) or PVP under the same conditions (Fig. S5), it was surprisingly found that the morphological structure of the Co_2Ni_2 ANCs presented a completely different consequence with orderly arranged four-pointed stars with average size of 50nm (Fig. S5a-c, CTAB) and average intact branch of 500nm (Fig. S5d-f, PVP), respectively. The main reason may be related with a weakly base environment provided by the urea rather than CTAB and PVP, which is the necessary for self-assembly of cubic structure. It is demonstrated that the urea plays a decisive role in the growth of uniform nanocubes. Furthermore, the acetylacetone groups were acted as a template unit for the cluster assembly which was also evidenced by the experiment. The nano-cubic structure could not be obtained when $Ni(acac)_2$ and $Co(acac)_2$ were replaced with $NiCl_2$ and $CoCl_2$. In hydrothermal conditions, the hydrazine hydrate could be complexed with $Ni(acac)_2$ and $Co(acac)_2$ to form the $[CoNi(N_2H_4)_2(acac)_2]_n$ complex (Fig. S6) and the metal acetylacetone chains were further crosswise linked with hydrazine by the interaction of hydrogen bond (O···H─N). The acetylacetone groups were acted as a template unit for the cluster assembly[S1] and some of the metal ions in the complex were co-reducted by hydrazine hydrate to form face-centered cubic NiCo alloy nanonuclears. During the growth of NiCo alloy nanonuclears, the urea would selectively adsorbed on to the (111) crystal planes of face-centered cubic NiCo alloy nanoparticles, which is more active than other crystal planes. Therefore, the growth of the (111) crystal planes was promoted since the metals may coordinate with urea and facilitate the co-reduction of Ni or Co in the complex, while the other crystal planes were passivated[S2]. This is evidenced by XRD analysis, in presence of urea the peak of (111) crystal plane of NiCo alloy was much stronger than that in absence of urea (Fig. S7). Due to the intrinsic cubic structures, nanonuclears tend to grow and arrange

into NiCo alloy nanocubes by self-assembly to lower the energy of the system, resulting from the high surface energy of the nanocubes. Such formation mechanism was similar to that of the solvent coordination molecular template effect in the fabrication of iron nanocubes[37]. With the extension of the synthesis time, the thickness of the NiCo alloy nanocube will isotropically grow further and become denser owing to the strong magnetic interaction. Meanwhile, the metal ions in the core of the NiCo alloy nanocube decrease and the ligands from the reduced $[CoNi(N_2H_4)_2(acac)_2]_n$ complexes will be filled inside, which would lead to the formation of hollow structure in acid etch step.

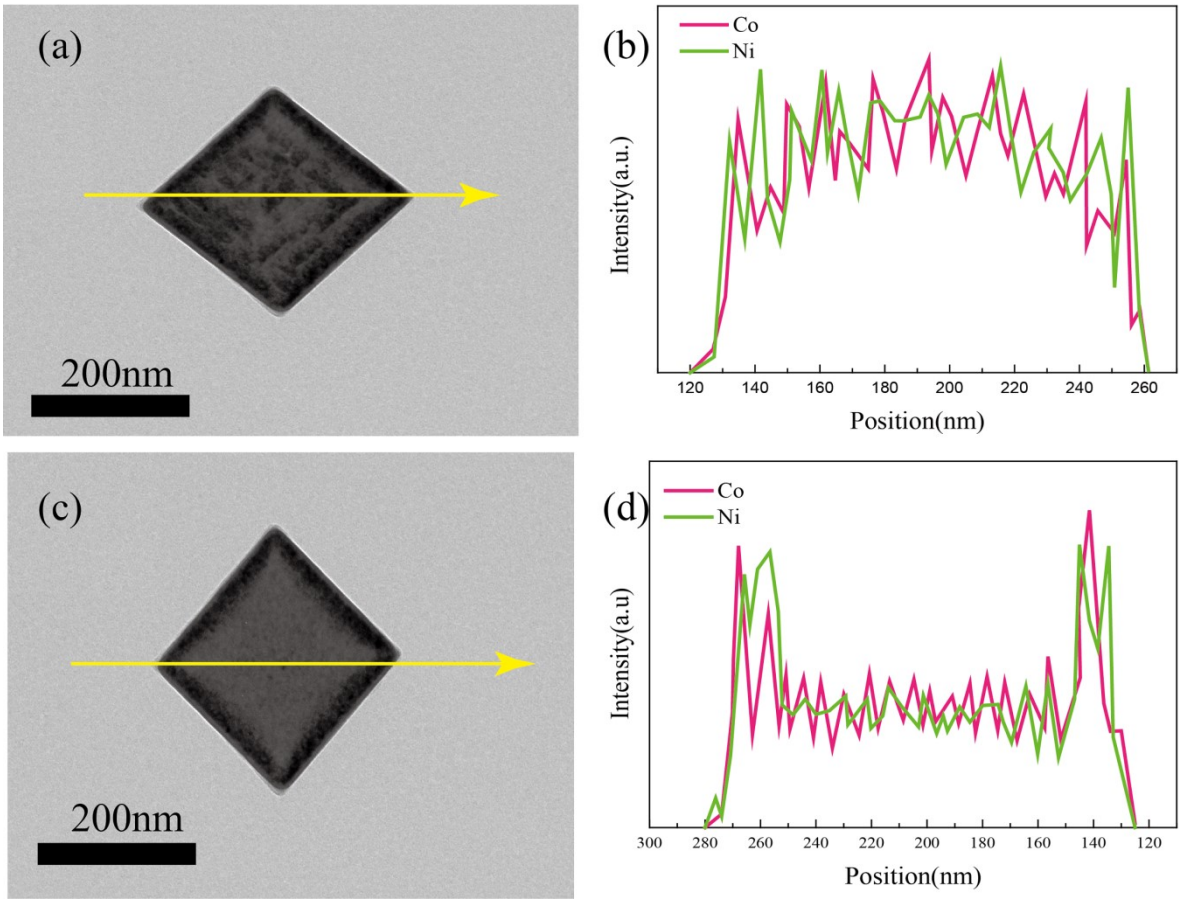

Figure S8 TEM images (a, c) and the corresponding STEM-EDS line-scanning profiles along the yellow lines (b, d) of Co_2Ni_2 ACNs and HACNs respectively.

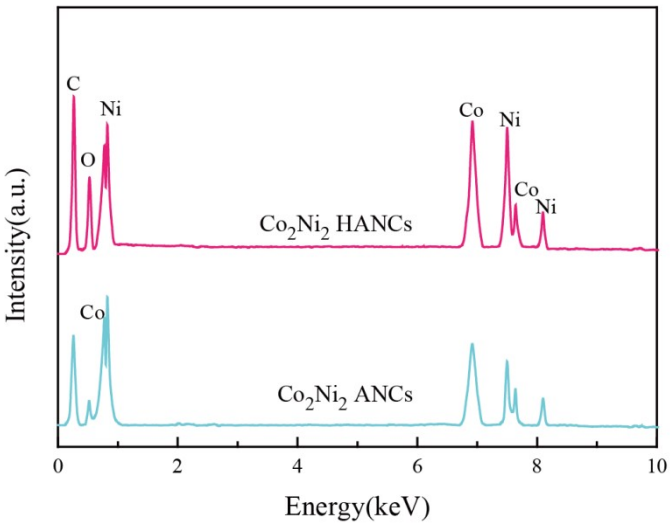

Figure S9 STEM-EDS analyses results of Co_2Ni_2 ACNs and HACNs.

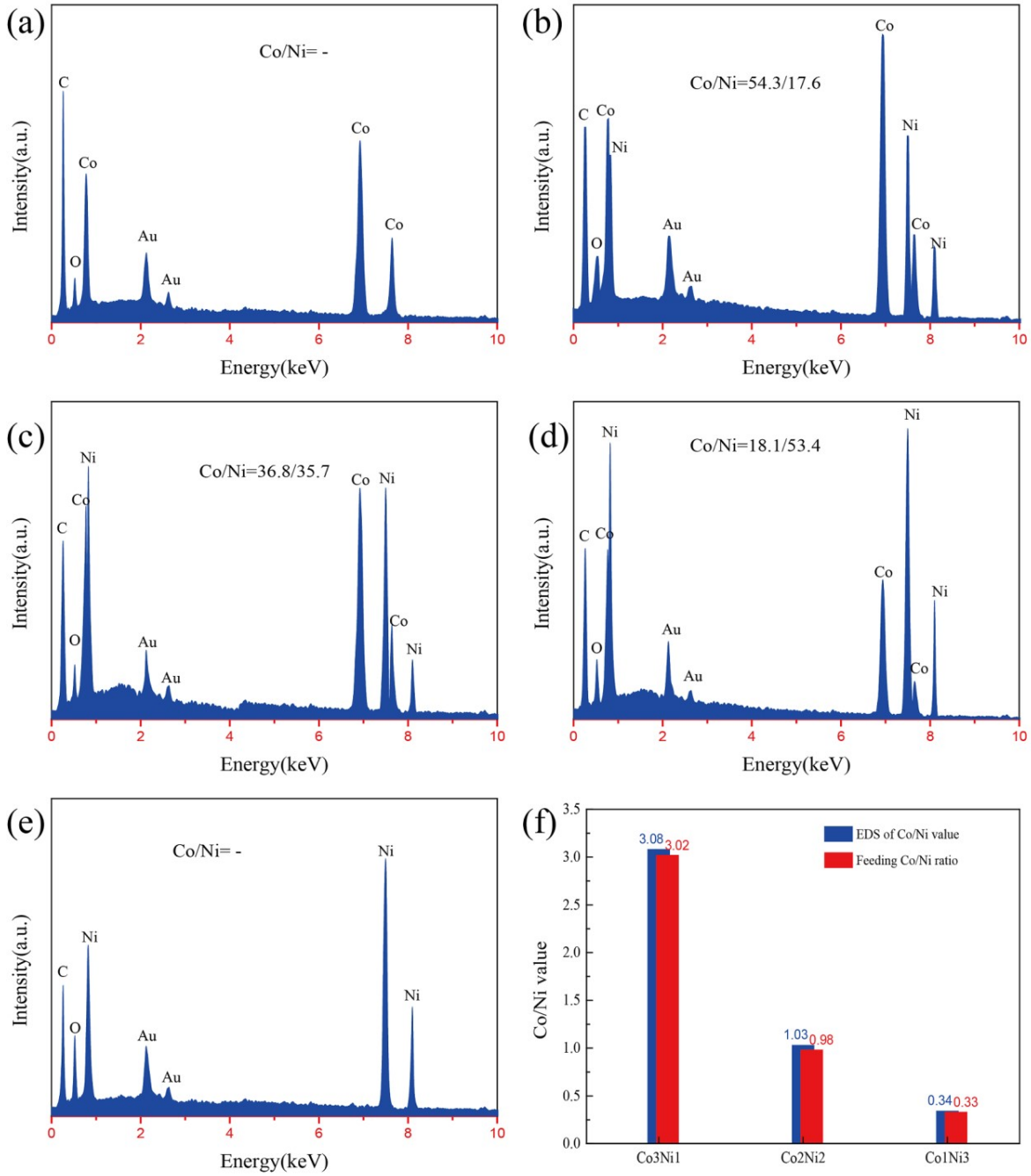

Figure S10 SEM-EDS analyses results of Co (a), Co_3Ni_1 (b), Co_2Ni_2 (c), Co_1Ni_3 (d) and Ni (e) ANCs and the comparisons of the EDS value with the feeding Co/Ni ratio for Co_3Ni_1, Co_2Ni_2 and Co_1Ni_3 ANCs.

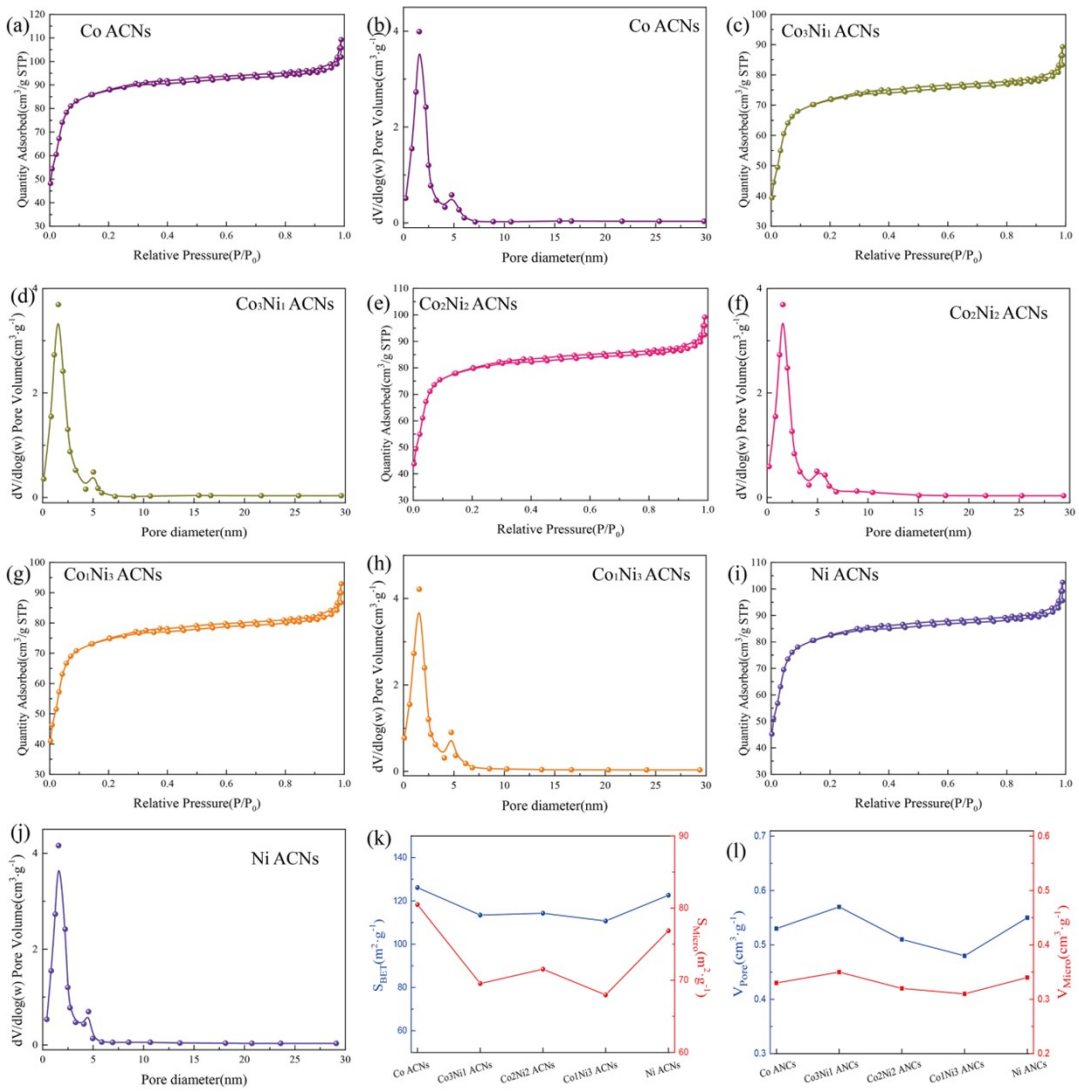

Figure S11 N_2 adsorption-desorption isotherms and the pore size distribution curves and (k) surface area ($m^2 \cdot g^{-1}$); (l) pore volume ($cm^3 \cdot g^{-1}$) of Co, Co_3Ni_1, Co_2Ni_2, Co_1Ni_3 and Ni ACNs.

The specific surface area and pore volume of HACNs obtained after acid etching are improved, which is conducive to the attachment of various molecular groups in the ORR catalytic process, thus accelerating the rate of ORR catalysis. As pore sizes become more abundant, the benefits of hierarchical porous materials become apparent.In addition, the specific surface area of micropores and the ratio of micropore volume in HACNs decreased sharply, from 63% of ACNs to about 13 and from 63% of ACNs to about 31%, respectively. This is caused by the acidification and washing of various particles in the catalyst material of the alloy and the disappearance of the agglomeration of excess unreflected metal ions.

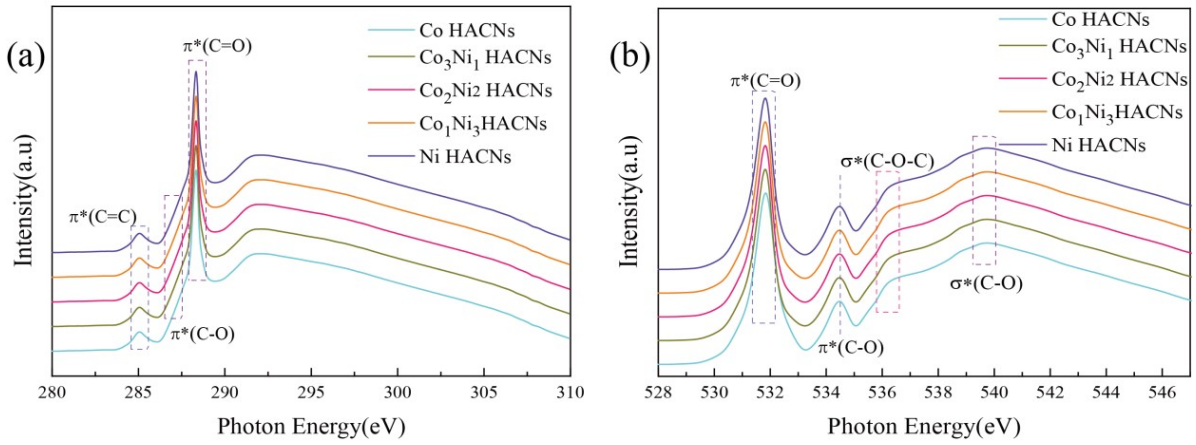

Figure S12 C and O K-edge XANES Co, Co_3Ni_1, Co_2Ni_2, Co_1Ni_3 and Ni HACNs.

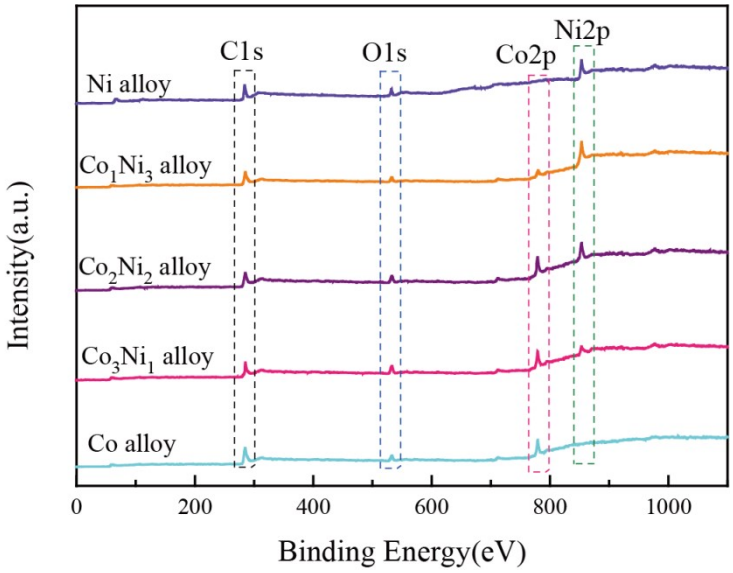

Figure S13 XPS survey of Co, Co_3Ni_1, Co_2Ni_2, Co_1Ni_3 and Ni HANCs.

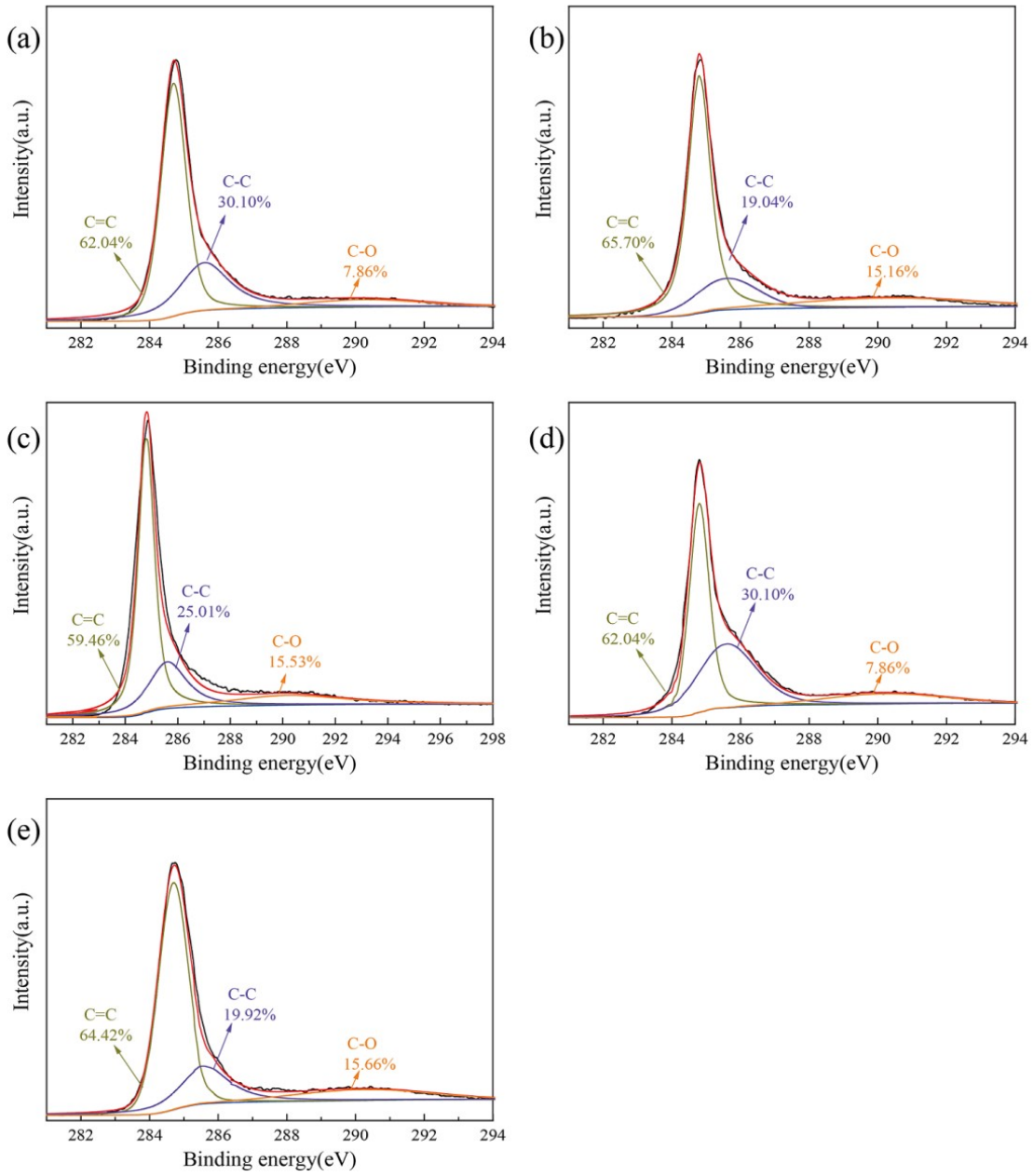

Figure S14 C 1s high-resolution XPS spectra of (a) Co, (b) Co_3Ni_1, (c) Co_2Ni_2, (d) Co_1Ni_3 and (e) Ni HACNs.

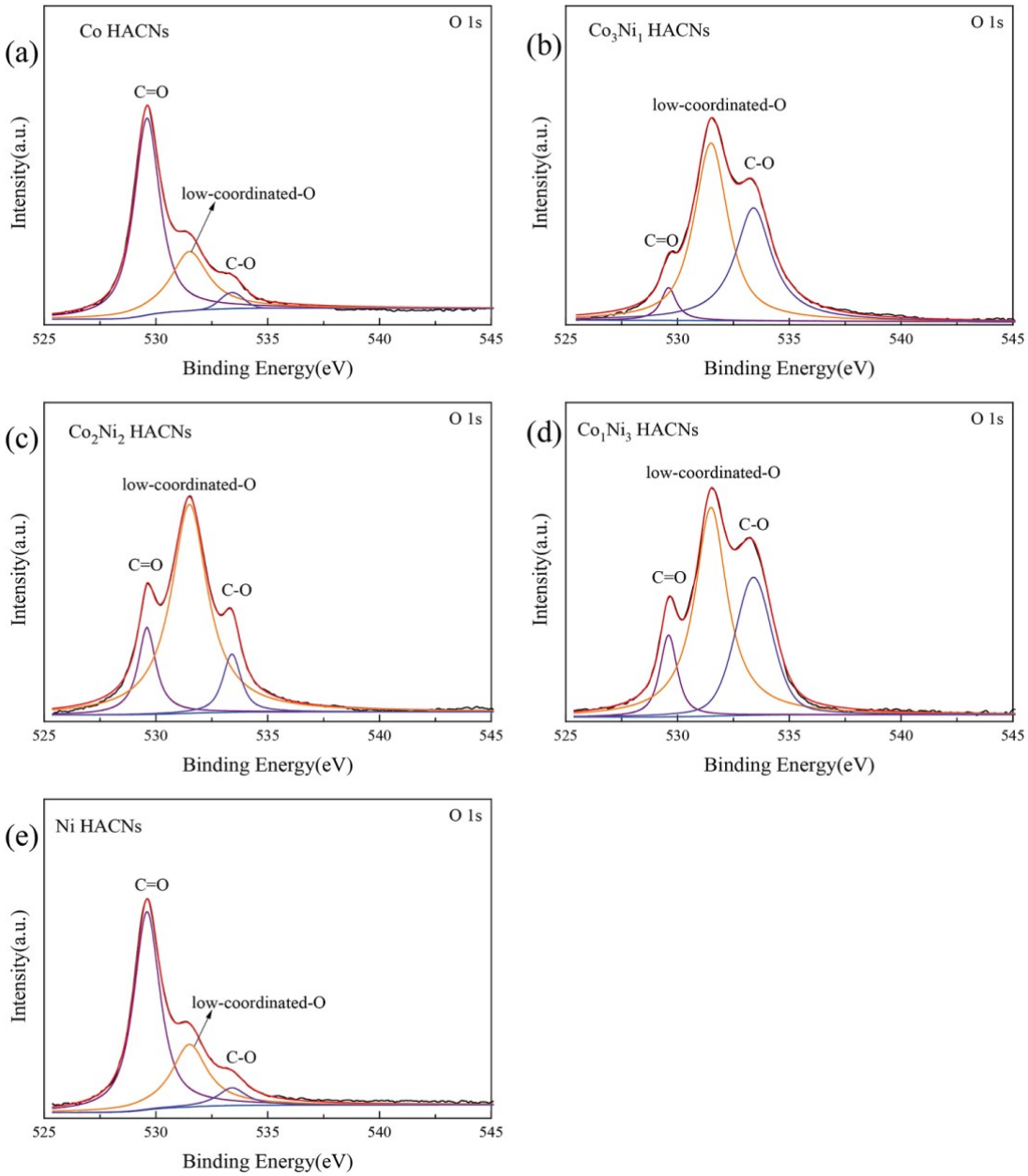

Figure S15 O 1s high-resolution XPS spectra of (a) Co, (b) Co_3Ni_1, (c) Co_2Ni_2, (d) Co_1Ni_3 and (e) Ni HACNs.

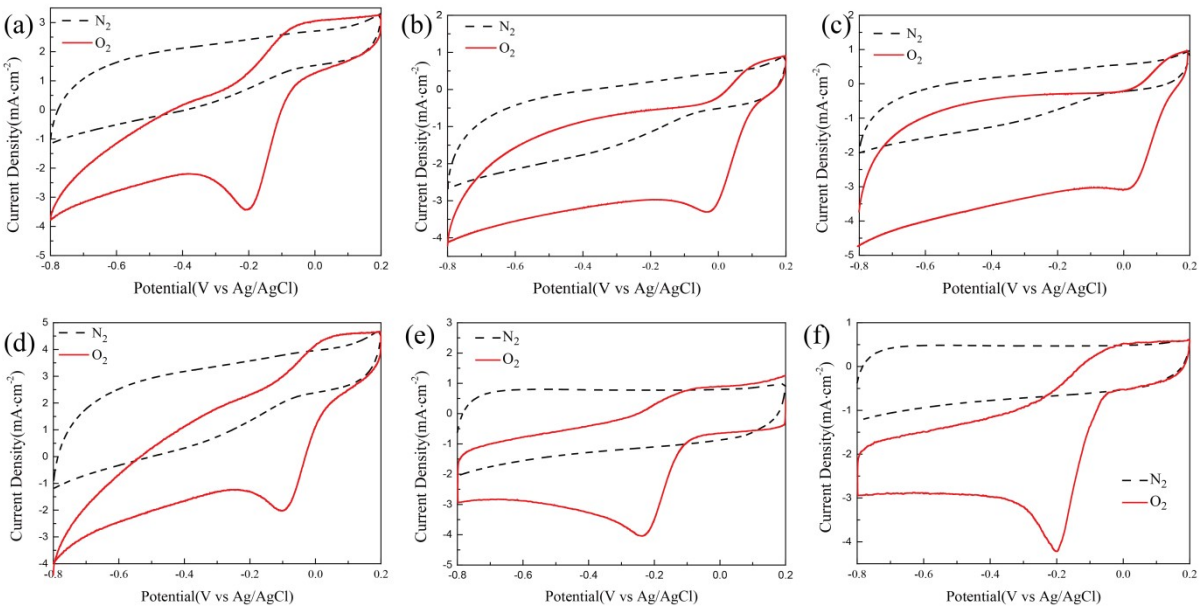

Figure S16 CV curves of Co (a), Co_3Ni_1(b), Co_2Ni_2(c), (d)Co_1Ni_3, (e)Ni HANCs and (f) Co_2Ni_2 ANCs in O_2 (solid) and N_2 (dash)-saturated 50 mM neutral phosphate buffer solution (PBS) medium with a scan rate of 50 $mV \cdot s^{-1}$.

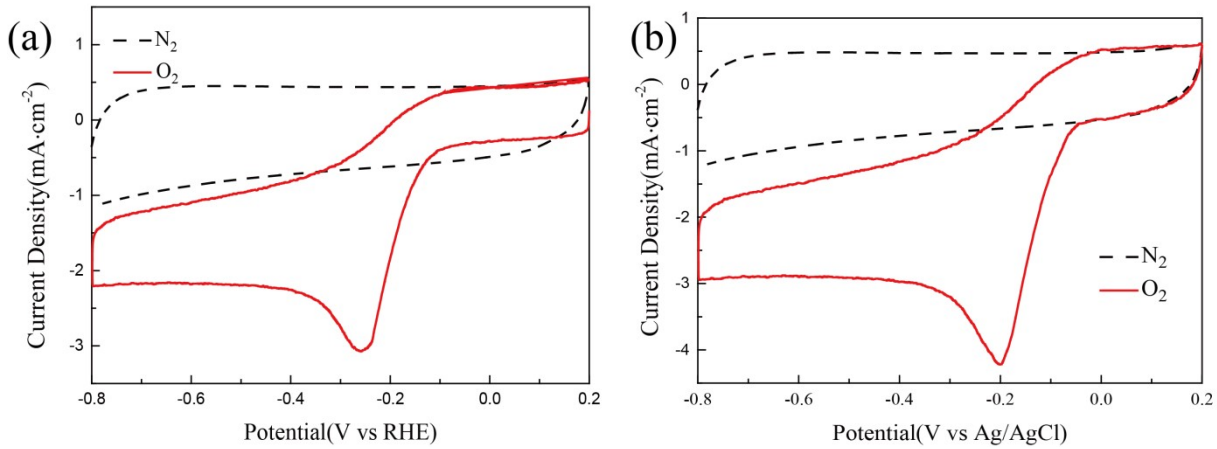

Figure S17 CV curves of Co_2Ni_2 particles (a) and Co_2Ni_2 ANCs in O_2 (solid) and N_2 (dash)-saturated 50 mM neutral phosphate buffer solution (PBS) medium with a scan rate of 50 $mV \cdot s^{-1}$.

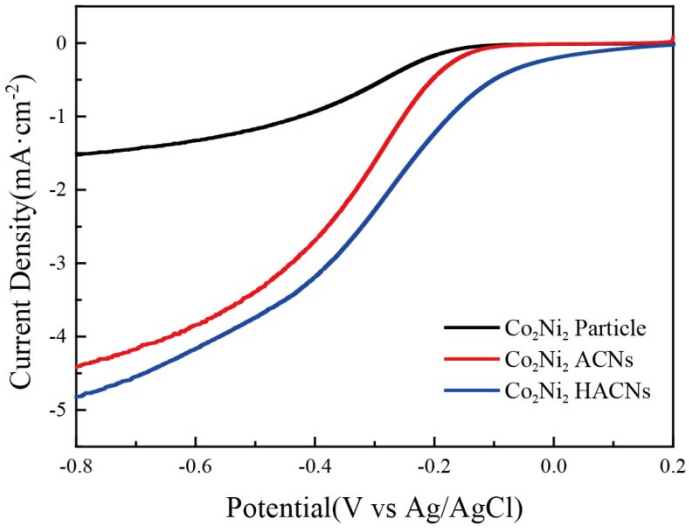

Figure S18 LSV curves of Co_2Ni_2 particles, ACNs and HACNs in the O_2-saturated 50 mM neutral phosphate buffer solution (PBS) medium at the rotation rate of 1600rpm.

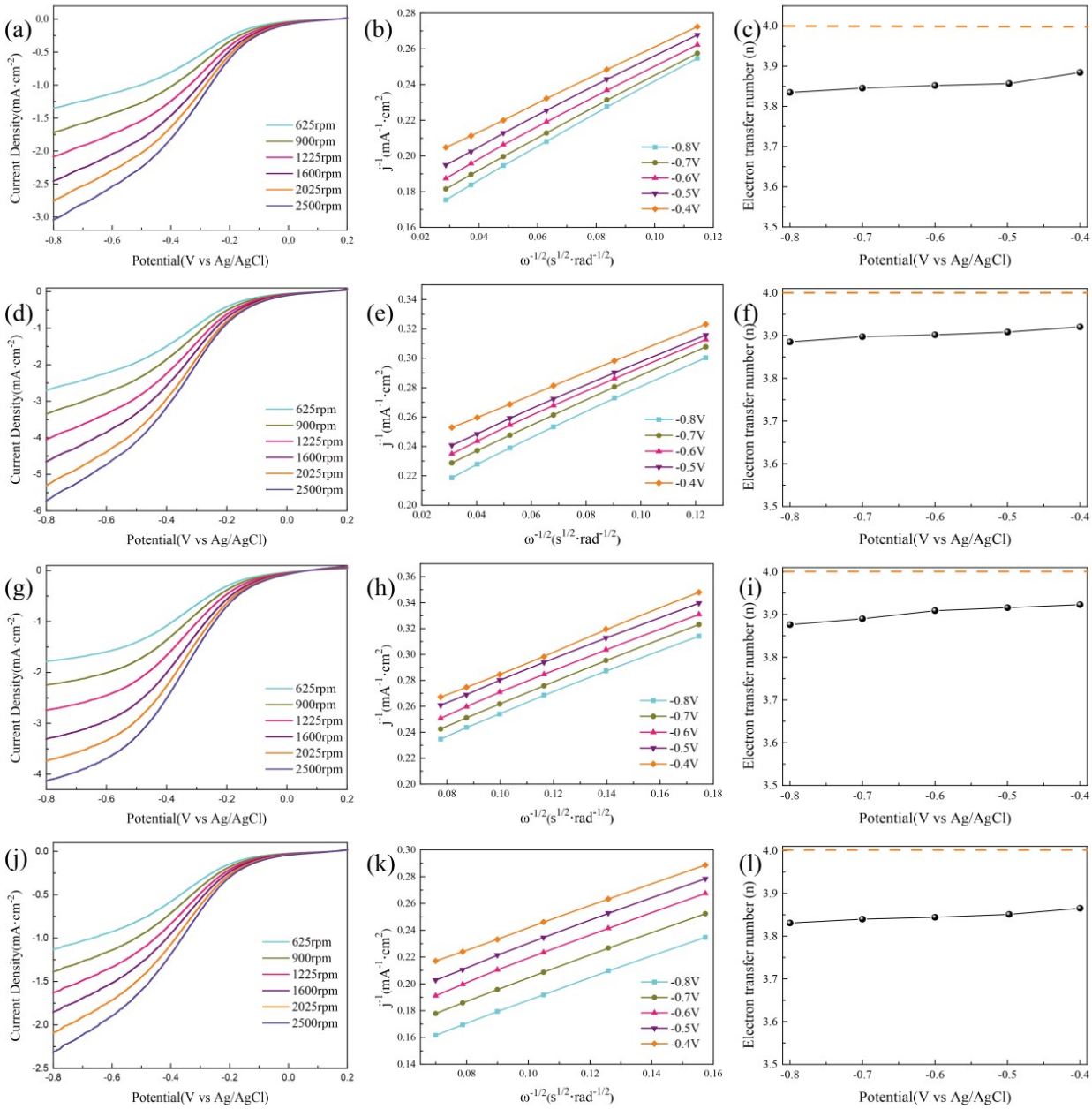

Figure S19 RDE-LSVtests under different rotating speeds (625-2500rpm), K-L plots and the corresponding calculated electron transfer number of Co (a-c), Co_3Ni_1(d-f), Co_1Ni_3(g-i) and Ni(j-l) HANCs in O_2-saturated 50 mM neutral phosphate buffer solution (PBS) medium with a scan rate of 50 $mV \cdot s^{-1}$.

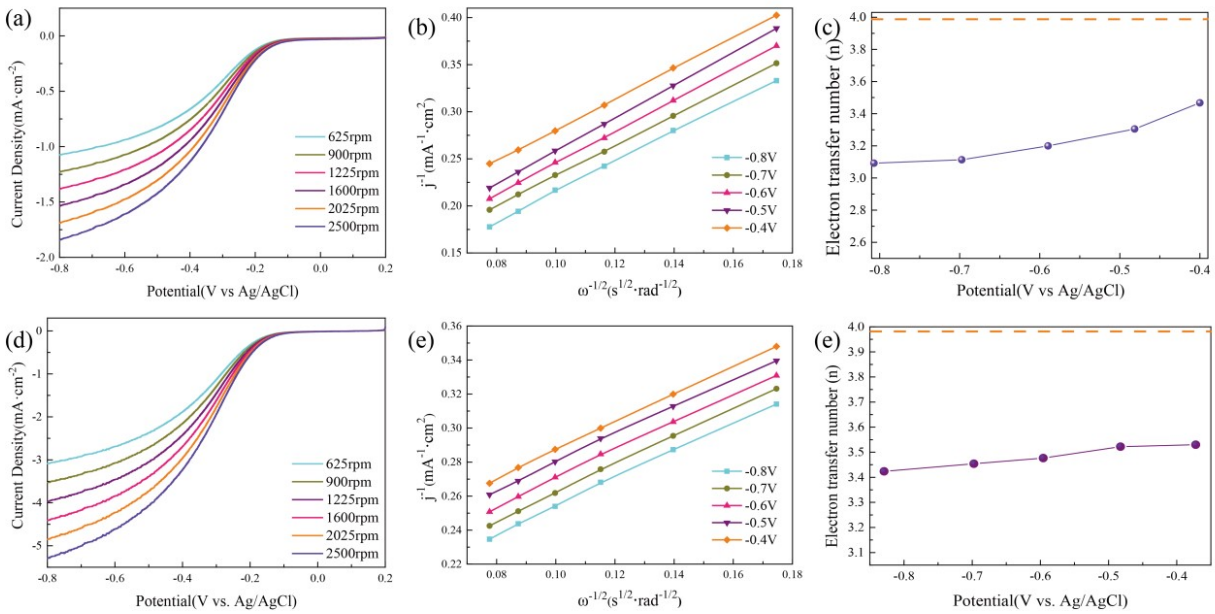

Figure S20 (a, d) RDE-LSVtests under different rotating speeds (625-2500rpm), (b, e) K-L plotsand the corresponding calculated electron transfer number (c, e) in O_2-saturated 50 mM neutral phosphate buffer solution (PBS) medium with a scan rate of 50 $mV \cdot s^{-1}$of Co_2Ni_2particles and ANCs, severally.

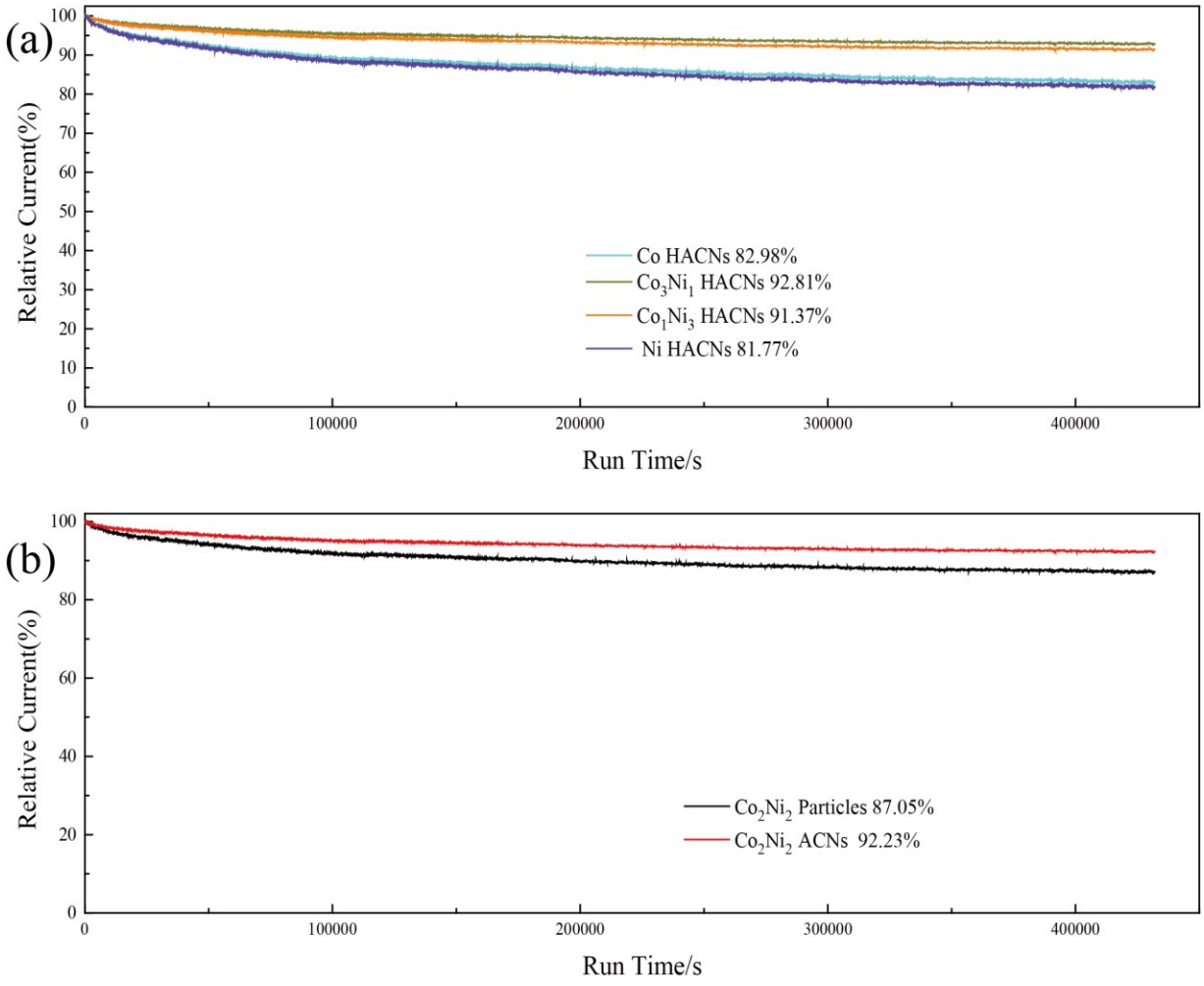

Figure S21Current retention curves of the various HACNs catalysts and Co_2Ni_2 particles and ACNs performed at -0.3 V in O_2 -saturated 50 mM neutral PBS medium.

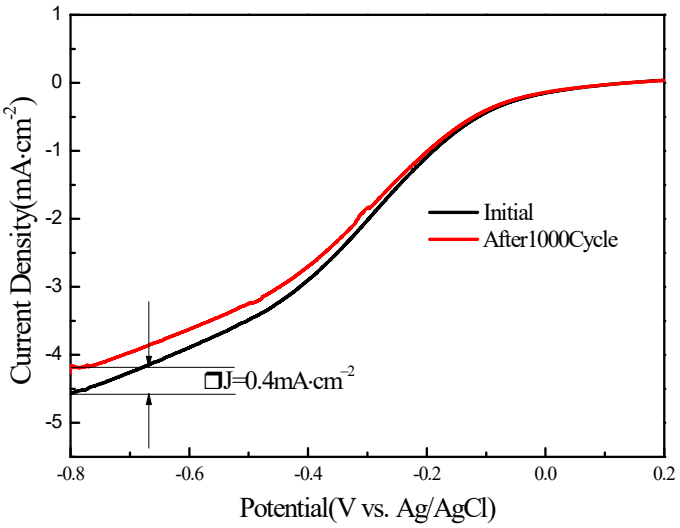

Figure S22 ORR polarization curves of Co_2Ni_2HACNs electrode tested after 1 and 1000 CV cycles.

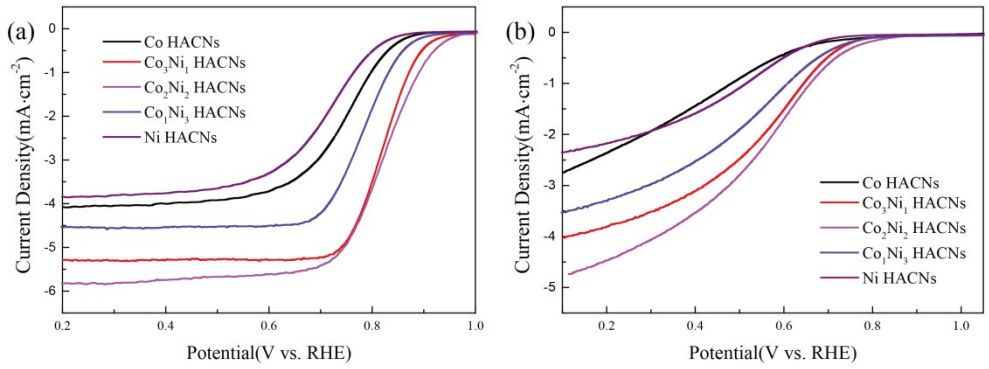

Figure 23 LSV curves of Co_xNi_y HACNs catalysts in O_2-saturated 0.1 mol·l^{-1} KOH solution (a) and O_2-saturated 0.1 mol·l^{-1} $HClO_4$ solution (b).

It can be found that the ORR activity of Co_2Ni_2 HACNs catalyst is better than other HACNs with a positive onset potential of 0.98V vs. RHE and a $E_{1/2}$ of 0.82Vvs. RHE in O_2-saturated 0.1 mol·l^{-1} KOH solution. And similarly the Co_2Ni_2 HACNs catalyst processes an excellent ORR performance with a onset potential (E_{ORR}) of 0.85V *vs.* RHE andlimited current density (@0.2V *vs.* RHE) of -4.49mA·cm^{-2}. The results indicate that Co-Ni HACNs alloyed catalyst has excellent ORR electrocatalytic activity in acidic and alkaline solutions.

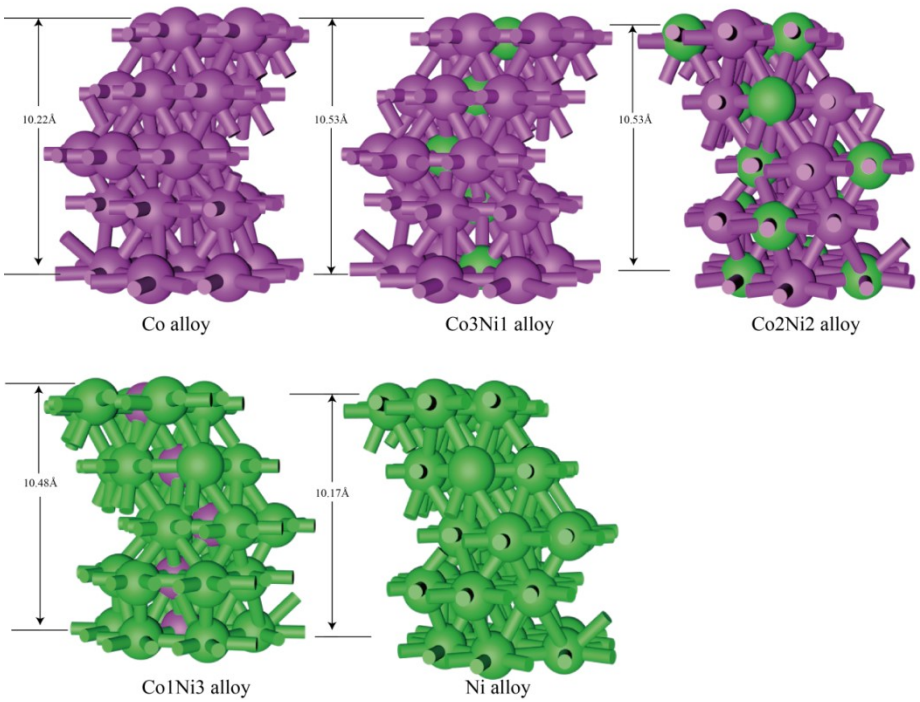

Figure S24 Optimized Models of Co_xNi_y alloy. Color code:green, Ni; violet, Co. The corresponding termination is (111) facet, and all models contain 5 mono-layers. For Co and Ni alloy, the compressive lattice strains of Co and Ni(111) facet of themare both 2.1%, respectively, relative to the lattice constant of pure Co and Nisubstance. Thecompressive lattice strains of other Co_xNi_y alloy of Co(111) facet is 0.5%. All 5 mono-layers were relaxed in the calculation. The totalthickness is around 10.50Å (1.05 nm) and the mono-layer for Co_xNi_y alloy is 2.1Å (0.21nm), inconsistent with the experimentally synthesized catalysts.

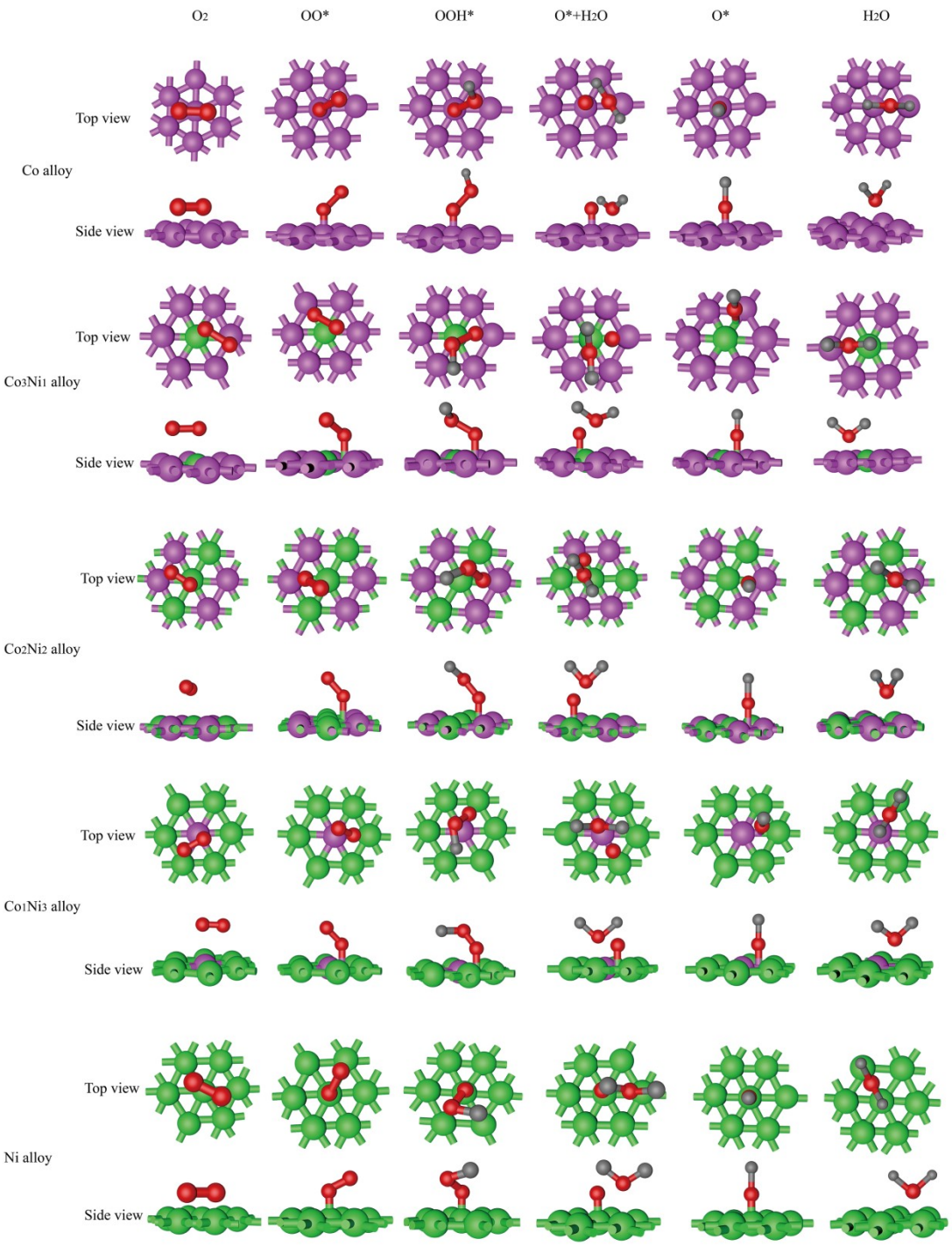

Figure S25 Optimized atomic configurations of oxygen intermediates (OOH*, O* and OH*) adsorbed on Co_xNi_y alloy.The top and side view of the optimized Co_xNi_y alloy.

Top and bottoms panelsshow the projection and lateral views of the adsorption configurations, respectively. In the figure, gray balls represent H atoms,green balls represent Ni atoms, violet ballsrepresent Co atoms, and red balls represent O atoms.

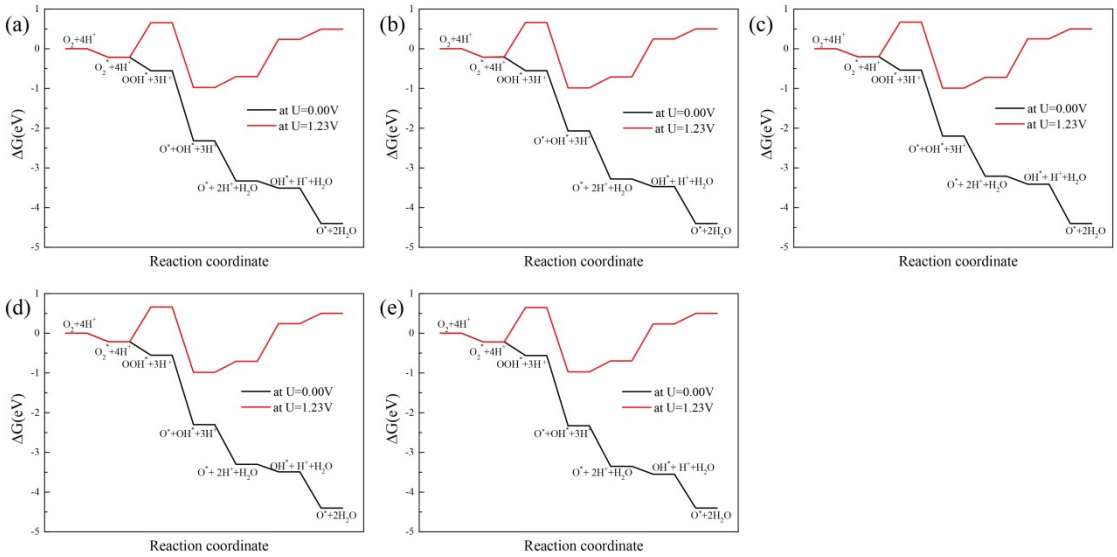

Figure S26 DFT-determined potential energy profiles of ORR over Co(a), Co_3Ni_1(b), Co_2Ni_2(c), Co_1Ni_3(d) and Ni(e) alloy via the associative mechanism.

The overpotential for ORR over Co, Co_3Ni_1, Co_2Ni_2, Co_1Ni_3 and Ni alloy is 1.10, 1.02, 0.99, 1.04 and 1.13eV, respectively.Furthermore, the overpotential for ORR of Co_2Ni_2 alloy is extremely closer to that of Pt(111) facet determining the electrocatalysis of ORR(0.99)[S3], show that the ORR catalytic activity of the Co_2Ni_2 is as good as that of Pt (111).

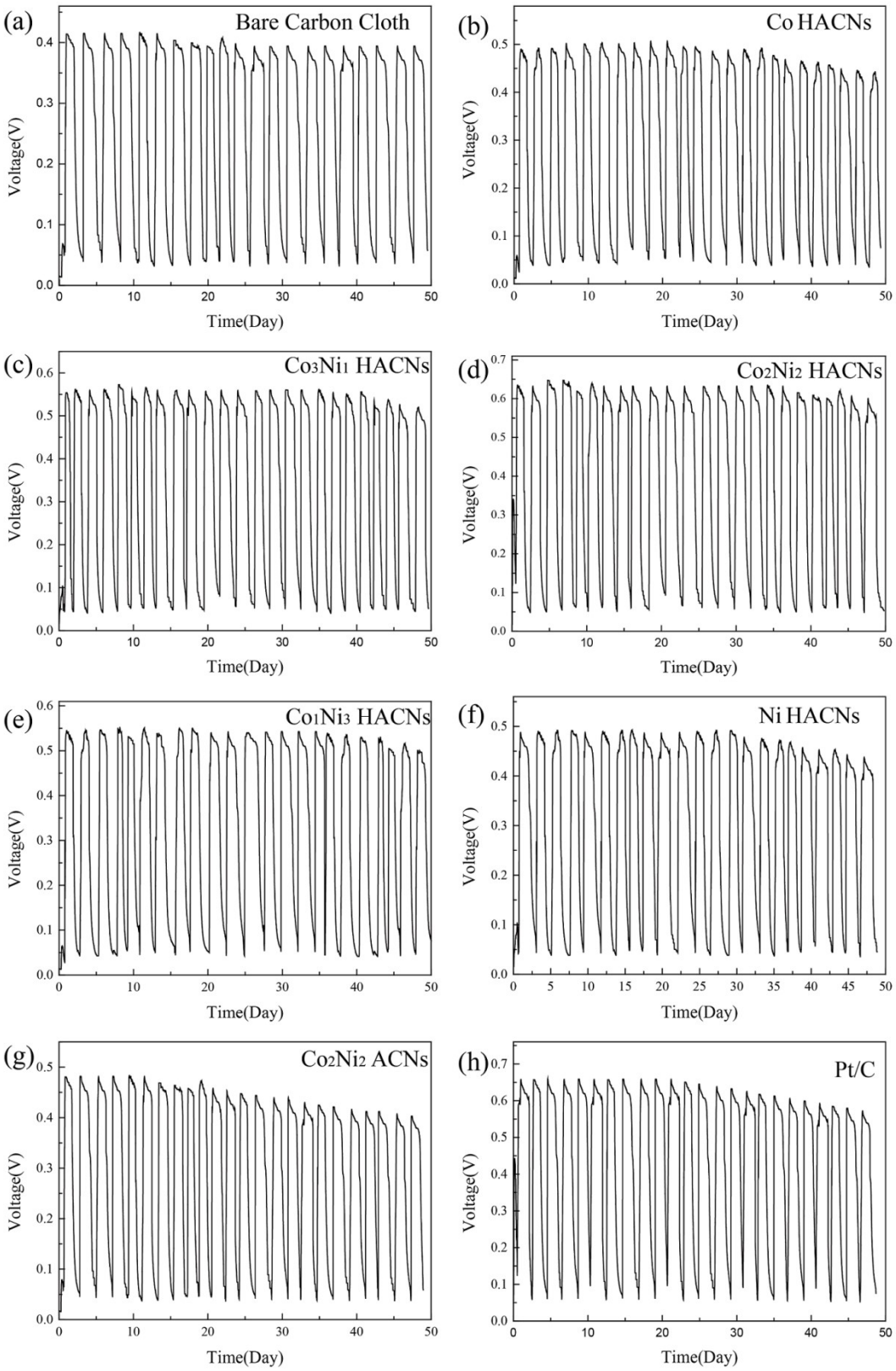

Figure S27 Voltage output of MFCs with (a) bare carbon cloth (CC), (b)Co, (c)Co_3Ni_1, (d) Co_2Ni_2,(e) Co_1Ni_3, (f) Ni HACNs, (g) Co_2Ni_2 ACNs and Pt/C cathodes throughout the whole operation cycles.

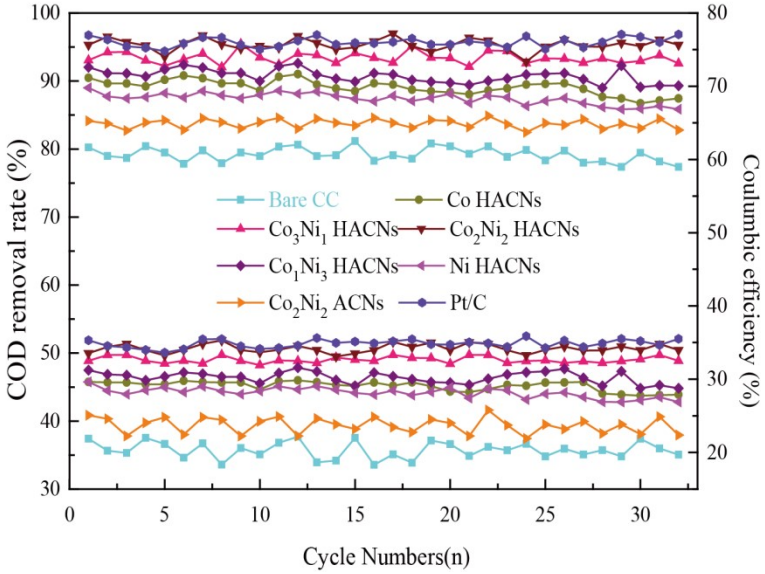

Figure S28 Water treatment performance reflected in COD removal rate and CEs.

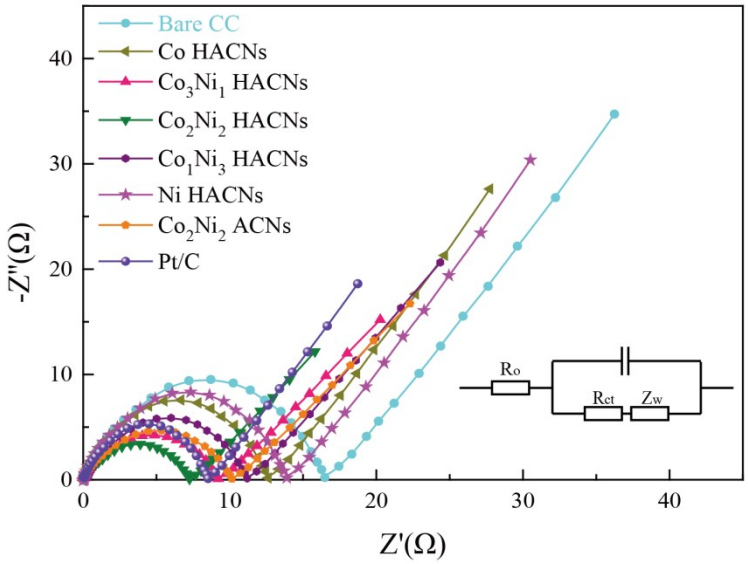

Figure S29 Nyquist curves (the inseted is the equivalent circuit (EC)) of all catalysts-MFCs.

Table S1 Elemental composition analyze results of Co, Co_3Ni_1, Co_2Ni_2, Co_1Ni_3 and Ni ANCs via SEM-EDS and TEM-EDS.

Samples	SEM-EDS (wt%)					TEM-EDS (wt%)				
	C	O	Co	Ni	Co/Ni	C	O	Co	Ni	Co/Ni
Co	20.4	6.3	73.3	-	-	17.2	5.2	77.6	-	-
Co_3Ni_1	21.6	6.5	54.3	17.6	54.3/17.6	17.5	5.4	58.2	18.9	58.2/18.9
Co_2Ni_2	21.4	6.1	36.8	35.7	36.8/35.7	18.2	5.1	39.2	37.5	39.2/37.5
Co_1Ni_3	21.8	6.7	18.1	53.4	18.1/53.4	18.1	5.3	18.4	58.2	18.4/58.2
Ni	20.5	6.4	-	73.1	-	17.1	5.7	-	77.2	-

Table S2 Elemental composition analyze results of Co, Co_3Ni_1, Co_2Ni_2, Co_1Ni_3 and Ni HANCs via SEM-EDS, EA and ICP-OES.

Samples	SEM-EDS (wt%)				EA (wt%)				ICP-OES (wt%)	
	C	O	Co	Ni	C	O	Co	Ni	Co	Ni
Co	35.8	5.3	58.9	-	39.6	6.2	75.2	-	100	-
Co_3Ni_1	35.6	5.5	45.1	13.8	38.4	5.8	41.5	14.3	75.7	24.3
Co_2Ni_2	35.5	5.1	19.2	21.4	38.9	6.3	27.9	26.9	50.4	49.6
Co_1Ni_3	35.6	5.7	14.1	44.6	38.7	6.4	41.6	57.4	25.3	74.7
Ni	36.1	5.4	-	58.5	39.3	5.9	-	75.4	-	100

Table S3 Physicochemical properties of Co, Co_3Ni_1, Co_2Ni_2, Co_1Ni_3 and Ni ANCs.

Samples	Specific surface area($m^2 \cdot g^{-1}$)			Pore volume($cm^3 \cdot g^{-1}$)			D
	S_{BET}	S_{Micro}	S_{Micro}/S_{BET}	V_{Pore}	V_{Micro}	V_{Micro}/V_{Pore}	(nm)
Co ACNs	126.15	80.48	63.8%	0.53	0.33	62.2%	3.07
Co_3Ni_1 ACNs	113.45	69.54	61.2%	0.57	0.35	61.4%	3.12
Co_2Ni_2 ACNs	114.28	71.53	62.6%	0.51	0.32	62.7%	3.06
Co_1Ni_3 ACNs	110.71	67.97	61.4%	0.48	0.31	64.5%	3.13
Ni ACNs	122.59	76.86	62.7%	0.55	0.34	61.8%	3.11

S_{BET}: Specific surface area, S_{Micro}: Micropore surface area, V_{Pore}: Pore volume, V_{Micro}: Micropore volume, D: Pore diameter.

Table S4 Physicochemical properties of Co, Co_3Ni_1, Co_2Ni_2, Co_1Ni_3 and Ni HANCs.

Samples	Specific surface area($m^2 \cdot g^{-1}$)			Pore volume($cm^3 \cdot g^{-1}$)			D
	S_{BET}	S_{Micro}	S_{Micro}/S_{BET}	V_{Pore}	V_{Micro}	V_{Micro}/V_{Pore}	(nm)
Co	432.35	65.37	15.1%	0.88	0.27	31.3%	7.09
Co_3Ni_1	354.17	48.21	13.6%	0.82	0.26	31.7%	7.26
Co_2Ni_2	387.25	51.95	13.4%	0.85	0.25	29.6%	7.15
Co_1Ni_3	376.47	49.38	13.1%	0.84	0.26	31.1%	7.21
Ni	400.94	59.26	14.8%	0.86	0.27	31.6%	7.13

S_{BET}: Specific surface area, S_{Micro}: Micropore surface area, V_{Pore}: Pore volume, V_{Micro}:Micropore volume, D: Pore diameter.

Table S5 Summary of element contents for C, O, Co, Ni and Co/Ni ratio in Co, Co_3Ni_1,Co_2Ni_2, Co_1Ni_3, Ni HANCs and Co_2Ni_2 HANCs determined by XPS measurements.

Samples	Surface content (at%)					Ratio of $M^{(0)}/M^{(II)}$(%)	
	C	O	Co	Ni	Co/Ni value	$Co^{(0)}/Co^{(II)}$	$Ni^{(0)}/Ni^{(II)}$
Co	27.3	5.1	67.6	-	-	69.7	-
Co_3Ni_1	27.1	5.2	54.6	15.7	59.6/20.7	38.6	54.9
Co_2Ni_2	25.7	5.8	34.7	37.6	39.7/42.6	44.5	68.3
Co_1Ni_3	26.5	5.3	14.3	53.9	19.3/58.9	37.4	51.4
Ni	26.8	4.7	-	68.5	-	-	79.5

Table S6 The fraction of oxygen speciesin Co, Co_3Ni_1, Co_2Ni_2, Co_1Ni_3, Ni HANCs and Co_2Ni_2 HANCs determined by XPS measurements.

	Ratio of different oxygen species (%)		
	Stoichiometric oxygen	Low-coordinated oxygen	Surface adsorbate oxygen
Co	65.8	30.7	3.5
Co_3Ni_1	4.8	54.6	40.6
Co_2Ni_2	15.2	75.2	9.6
Co_1Ni_3	11.7	52.5	35.8
Ni	61.5	27.9	10.6

Table S7 Summary of element state of binding shift in Co, Co_3Ni_1, Co_2Ni_2, Co_1Ni_3, Ni HANCs and Co_2Ni_2 HANCs determined by XPS measurements.

Samples	Element state of binding energy shift (eV)			
	$Co2p_{1/2}$	$Co2p_{3/2}$	$Ni2p_{1/2}$	$Ni2p_{3/2}$
Co	-	-	-	-
Co_3Ni_1	0.14	0.13	2.1	1.9
Co_2Ni_2	0.26	0.20	1.3	1.5
Co_1Ni_3	0.43	0.37	0.7	0.8
Ni	-	-	-	-

Table S8 Comparison of performance toward ORR of Co, Co_3Ni_1, Co_2Ni_2, Co_1Ni_3, Ni HANCs and Co_2Ni_2 ANCs.

Samples	E_{onset}(V)	$E_{1/2}$ (V)	J_d(mA·cm^{-2})
Co HANCs	-0.04	-0.35	-2.45
Co_3Ni_1 HANCs	0.12	-0.37	-4.66
Co_2Ni_2 HANCs	0.15	-0.32	-4.58
Co_1Ni_3 HANCs	0.07	-0.31	-3.28
Ni HANCs	-0.05	-0.38	-1.85
Co_2Ni_2 ANCs	-0.02	-0.35	-1.52
20% Pt/C	0.16	-0.32	-5.32

E_{onset}:Onset potential, $E_{1/2}$: half-wave potential, J_d :Limited Current(J@-0.8Vvs.Ag/AgCl).

Table S9 Comparison of our work with reported electrochemical data

Catalyst	E_{onset}V vs. Ag/AgCl	$E_{1/2}$ V vs. Ag/AgCl	J_d(mA·cm^{-2})	Ref.
Co_2Ni_2	0.15	-0.22	-4.58	This work
Pt/C	0.16	-0.32	-5.32	This work
NC@CoNC/rGO-15	0.13	0.02	-3.4	[S4]
$NFe_{0.5}$-C	0.14	-0.26	4.24	[S5]
N-C	0.108	-0.31	-4.61	[S5]
MOF-900	0.115	-0.37	−2.94	[S6]
MOF-800	0.106	-0.37	-3.26	[S6]
Ag/Fe/N/C-630	0.21	-0.21	-1.4	[S7]
$Fe/Fe_3O_4/Fe_3C$/NPGC640	0.16	-0.16	-0.13	[S8]
Co_3O_4/N-G	0.14	-0.24	-4.21	[S9]

Table S10 DFT-determined potential energy values of intermediates of ORR over Co_xNi_y alloy at T=300K.

Species	E(eV)	S(J·K^{-1})	TS(eV)	ZPE(eV)	CvT(eV)	G(eV)	ΔG(eV)
O_2	-9.86	205.329	0.638	0.099	0.049	-10.3505	
H_2O	-14.23	189.042	0.588	0.567	0.05	-14.2008	
H_2	-6.7	130.858	0.407	0.304	0.019	-6.7839	
Co Alloy							
O_2+4H$^+$	-72.09		0.555	0.054	0.219	-72.181	0
O_2*+4H$^+$	-82.76		0.594	0.193	0.253	-82.742	-0.21
OOH*+3H$^+$	-86.72		0.671	0.442	0.286	-86.745	-0.39
O*+OH*+3H$^+$	-88.38		0.577	0.245	0.265	-88.375	-1.84
O*+2H$^+$+H_2O	-82.16		0.583	0.329	0.232	-82.147	-1.21
OH*+H$^+$+H_2O	-77.82		0.589	0.325	0.221	-77.824	-0.13
2H_2O	-72.09		0.555	0.054	0.219	-72.181	-1.21
Co_3Ni_1 alloy							
O_2+4H$^+$	-110.67		0.532	0.067	0.221	-110.612	0
O_2*+4H$^+$	-115.03		0.536	0.217	0.255	-115.057	-1.42
OOH*+3H$^+$	-116.99		0.681	0.451	0.293	-116.942	-0.92
O*+OH*+3H$^+$	-123.65		0.585	0.483	0.267	-123.605	-2.77
O*+2H$^+$+H_2O	-117.43		0.564	0.148	0.245	-117.432	-1.96
OH*+H$^+$+H_2O	-121.24		0.550	0.409	0.236	-121.357	-0.21
2H_2O	-110.67		0.532	0.067	0.221	-110.612	-1.17
Co_2Ni_2 alloy							
O_2+4H$^+$	-109.26		0.527	0.065	0.218	-109.934	0
O_2*+4H$^+$	-113.62		0.528	0.212	0.251	-113.193	-0.23

OOH^*+3H^+	-117.58	0.665	0.491	0.285	-117.347	-0.41
$O^*+OH^*+3H^+$	-119.24	0.569	0.475	0.262	-119.351	-1.78
$O^*+2H^++H_2O$	-113.02	0.557	0.141	0.240	-113.26	-1.14
$OH^*+H^++H_2O$	-118.32	0.548	0.407	0.231	-118.564	-0.24
$2H_2O$	-109.26	0.527	0.065	0.218	-109.934	-1.15
			Co_1Ni_3 alloy			
O_2+4H^+	-113.16	0.535	0.068	0.223	-113.188	0
$O_2^*+4H^+$	-118.59	0.542	0.221	0.256	-118.565	-1.71
OOH^*+3H^+	-119.28	0.688	0.456	0.299	-119.471	-1.32
$O^*+OH^*+3H^+$	-125.29	0.591	0.488	0.272	-125.351	-3.24
$O^*+2H^++H_2O$	-120.78	0.572	0.153	0.252	-120.881	-1.61
$OH^*+H^++H_2O$	-122.54	0.558	0.412	0.239	-122.521	-0.19
$2H_2O$	-113.16	0.535	0.068	0.223	-113.188	-1.19
			Ni Alloy			
O_2+4H^+	-71.65	0.507	0.051	0.223	-71.181	0
$O_2^*+4H^+$	-78.47	0.498	0.192	0.261	-78.742	-0.18
OOH^*+3H^+	-78.64	0.527	0.439	0.299	-78.745	-0.35
$O^*+OH^*+3H^+$	-78.31	0.503	0.235	0.274	-78.375	-1.75
$O^*+2H^++H_2O$	-72.46	0.492	0.316	0.251	-72.147	-1.18
$OH^*+H^++H_2O$	-75.32	0.498	0.326	0.237	-75.824	-0.10
$2H_2O$	-71.65	0.507	0.051	0.223	-71.181	-1.17

Table S11 Performance results of Co, Co_3Ni_1, Co_2Ni_2, Co_1Ni_3, Ni HANCs, Co_2Ni_2 ANCs and Pt/C

Samples	$P_{max(W\cdot cm^{-2})}$		V_{OC}(V)		Maximum Cell Voltage(V)	
	Initial cycle	Last cycle	Initial cycle	Last cycle	Initial cycle	Last cycle
CC	0.51±0.03	0.43±0.03	0.94±0.02	0.85±0.01	0.41±0.02	0.39±0.01
Co HANCs	0.67±0.04	0.63±0.04	1.07±0.04	0.95±0.02	0.50±0.01	0.46±0.03
Co_3Ni_1 HANCs	0.93±0.03	0.83±0.03	1.18±0.02	0.97±0.03	0.57±0.02	0.52±0.04
Co_2Ni_2 HANCs	1.03±0.01	0.97±0.02	1.24±0.01	1.06±0.04	0.63±0.01	0.60±0.02
Co_1Ni_3 HANCs	0.85±0.04	0.78±0.01	1.12±0.03	0.96±0.02	0.54±0.02	0.50±0.04
Ni HANCs	0.69±0.02	0.65±0.04	1.02±0.04	0.94±0.01	0.49±0.01	0.44±0.03
Co_2Ni_2 ANCs.	0.57±0.03	0.50±0.03	0.98±0.01	0.88±0.02	0.48±0.02	0.41±0.03
20% Pt/C	1.11±0.02	0.88±0.02	1.25±0.03	1.03±0.01	0.64±0.04	0.57±0.03

Table S12 Water treatment and Electrochemical impedance fitting results of Co, Co_3Ni_1, Co_2Ni_2, Co_1Ni_3, Ni HANCs and Co_2Ni_2 ANCs

Samples	COD removal rate(%)		CEs(%)		R(Ω)	
	Initial cycle	Last cycle	Initial cycle	Last cycle	R_o	R_{ct}
CC	80.23±1.3	78.35±0.7	19.54±0.9	19.07±0.12	16.61±0.2	17.54±0.4
Co HANCs	90.25±1.1	88.11±0.4	29.44±1.3	27.62±1.2	12.61±0.3	14.42±0.3
Co_3Ni_1 HANCs	93.76±0.7	92.35±1.4	32.15±1.2	31.67±0.8	8.97±0.3	11.35±0.1
Co_2Ni_2 HANCs	96.27±1.2	95.36±1.4	34.58±1.1	33.27±0.9	7.25±0.5	9.36±0.2
Co_1Ni_3 HANCs	91.16±1.2	89.34±1.5	30.31±0.8	29.17±0.7	11.11±0.3	13.26±0.4
Ni HANCs	87.89±1.5	86.52±1.2	28.46±1.3	27.56±1.3	13.88±0.4	13.67±0.1
Co_2Ni_2 ANCs.	83.76±1.1	82.54±0.9	23.55±1.4	22.15±0.9	10.16±0.1	10.39±0.3
20% Pt/C	96.43±1.2	94.52±0.7	35.47±1.3	34.16±1.5	8.71±0.2	10.65±0.2

Reference

[S1] A. J. Ricco, R. M. Crooks, G. C. Osbourn, *Acc. Chem. Res.* **1998**, *31*, 28.

[S2] B. Qi, D. Li, X. Ni, H. Zheng, *Chem. Lett*. **2007**, *36*, 722.

[S3] X. Tian, X. Zhao, Y. Q. Su, L. Wang, H. Wang, D. Dang, B. Chi, H. Liu, E. J. M. Hensen, X. W. Lou, B. Y. Xia, *Science* **2019**, *366*, 850.

[S4] C.Zhao, Z.Qiu, J. Yang, Z. D. Huang, X.Shen, Y. Li, Y. Ma, *ACS Sustainable Chem. Eng.* ***2020****.*

[S5] J. Liu, L. Wei, C. Cao, F. Zhang, F. Lang, H. Wang, H. Yang, J. Shen, *Nanoscale*, **2019**,*11*, 13431.

[S6] L. Zhang, Y. Hu, J. Chen, W. Huang, J.Cheng, Y. Chen, *J. Power Sources*, **2018**, *384*, 98.

[S7] Y. Dai, Y. Chan, B. Jiang, L. Wang, J.Zou, K. Pan, H. Fu, *ACS Appl. Mater. Interfaces***2016**, *8*, 6992.

[S8] Y. Chan, Y.Dai, R. Li, J.Zou, G.Tian, H. Fu, *Carbon*,**2015**, *89*, 8.

[S9] Y. Su, Y. Zhu, X. Yang, J.Shen, J. Lu, X. Zhang, J. Chen, C. Li, *Ind. Eng. Chem. Res.***2013**, *52*, 6076.